Journal of Atmospheric and Solar–Terrestrial Physics 256 (2024) 106197

Contents lists available at ScienceDirect

Journal of Atmospheric and Solar–Terrestrial Physics

journal homepage: www.elsevier.com/locate/jastp

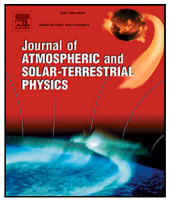

Research paper

On the strength of E and F region irregularities for GNSS scintillation in the dayside polar ionosphere

Mahith Madhanakumar [a,*], Andres Spicher [a], Juha Vierinen [a], Kjellmar Oksavik [b,c]

[a] Department of Physics and Technology, UiT The Arctic University of Norway, Tromsø, Norway
[b] Department of Physics and Technology, University of Bergen, Norway
[c] Arctic Geophysics, University Centre in Svalbard, Longyearbyen, Norway

ARTICLE INFO

Keywords:
Ionospheric scintillation
Dayside auroral/cusp region
EISCAT
GNSS

ABSTRACT

We present results of the study conducted to quantify the relative contribution of different ionospheric regions to phase scintillation in Global Navigation Satellite Systems (GNSS) at the dayside high latitude ionosphere. By taking advantage of the scanning capability of the 32-m EISCAT radar in Svalbard (ESR) and its recurrent favourable location below the dayside auroral region, we developed a methodology to identify conjunctions between the radar and GNSS satellite signals in order to compare density irregularities identified by the radar with scintillation observed in GNSS signals. The analysis revealed that the dayside ionosphere contained irregularities predominantly in the F region with scintillation occurring 77% of the times. The likelihood of observing irregularities in the E region were comparatively less with a scintillation occurrence rate of 42%. The study therefore strongly suggests that the dayside F region is more structured than the E region and is the predominant source region for irregularities that cause scintillation at GNSS frequencies. The associated ionospheric conditions revealed enhanced F region electron and ion temperatures to be collocated with scintillation for majority of the times. This supports the fact that cusp/auroral dynamics play a crucial role in creating F region irregularities which can act as sources of scintillation in GNSS signals. The presented results provide a quantitative estimate of the effectiveness of irregularities and the associated ionospheric conditions in different regions of the dayside ionosphere during scintillation, which are relevant for high latitude modelling and instability studies as well as for space weather applications.

1. Introduction

Electron density irregularities embedded in the ionospheric medium and their stochastic variability have long been attributed to causing disturbances on radio waves ranging from that of cosmic origin to that used by the Global Navigation Satellite Systems (GNSS) (Hey et al., 1946; Yeh and Liu, 1982; Kintner et al., 2007). These disturbances manifest themselves in the form of phase advance and group delays in addition to introducing diffractive and refractive variations in the amplitude and phase of a radio signal (Won and Lee, 2005). This, at times, can have adverse effects on the performance of applications that rely on radio propagation through the ionosphere (e.g. Kintner et al., 2007). The diffractive fluctuations are induced in a radio signal by Fresnel-scale sized electron density inhomogeneities, which is of the order of ~ 350 m at L1 GPS frequency at an altitude of 350 km, and are termed scintillation (Yeh and Liu, 1982; Kintner et al., 2007). Refractive variations on the other hand are caused by both Fresnel and large-sized irregularities that are typically of the order of tens of km (Kintner et al., 2007). Scintillation being stochastic tends to have larger impact on degrading the performance of GNSS technologies as they cannot be mitigated whereas the refractive fluctuations could be corrected by using dual frequency measurements (Kintner et al., 2007; McCaffrey and Jayachandran, 2019).

Scintillation can be caused by irregularities that are either present in the E region or the F region or both. A number of studies reported the presence of enhanced phase and amplitude scintillation in relation to auroral substorm events, polar cap patches and energetic particle precipitation, which can be attributed to E and F region structures (De Franceschi et al., 2008; Alfonsi et al., 2011; Moen et al., 2013; Oksavik et al., 2015; Spogli et al., 2009; Smith et al., 2008; Prikryl et al., 2013, 2011; Forte et al., 2017). Jin et al. (2014, 2016) and van der Meeren et al. (2015) observed the highest GPS phase scintillation levels when polar cap patches entered the night-side auroral region (which is a combination of both E and F region irregularities) whereas cusp

* Corresponding author.
E-mail address: mahith.madhanakumar@uit.no (M. Madhanakumar).

https://doi.org/10.1016/j.jastp.2024.106197
Received 16 June 2023; Received in revised form 18 November 2023; Accepted 24 February 2024
Available online 2 March 2024

auroral dynamics without the presence of patches (E region structures alone) and polar cap patches away from the active cusp (F region structures only) gave rise to moderate and weak scintillation, respectively (Jin et al., 2017). Using the Swarm satellites and GNSS observations, Fæhn Follestad et al. (2020) reported the colocation of regions with severe phase scintillation and highly filamented field-aligned currents (FACs) at the dayside auroral region by assuming the altitude of the irregularities. Using conjunction measurements between SWARM and ground-based scintillation data at polar, auroral and low latitudes, Kotova et al. (2022) had statistically shown that the Ionospheric Plasma IRregularities (IPIR) index could be taken as an indicator of plasma variations at SWARM altitudes that can be associated with scintillation on the ground. Using GPS data from Ny-Ålesund, Jin et al. (2018) found the highest scintillation occurrence rate to be around magnetic noon except for December 2014 when the night-side occurrence rate exceeded that from the dayside. Forte et al. (2017) conducted experimental campaigns at auroral latitudes using the Tromsø UHF radar by following the GPS satellites, which allowed the authors to attribute the observed L band scintillation to irregularities in either the E or the F region in the evening sector. Furthermore, numerous studies reported from the nightside auroral sector predominantly associated GNSS scintillation to irregularities in the E region (Makarevich et al., 2021; Semeter et al., 2017; Sreenivash et al., 2020; Loucks et al., 2017; Enengl et al., 2023).

As discussed above, even though many case studies relating scintillation and their strength to different ionospheric regions exist, a statistical study providing a clear consensus on the dominant altitude of the irregularities, their effectiveness in causing scintillation as well as the associated ionospheric conditions in the dayside auroral/cusp region has yet to be established. This article therefore aims to address this knowledge gap by taking advantage of the collocated European Incoherent SCATer (EISCAT) Svalbard radar (ESR) at a latitude of 78.153° and longitude of 16.029°, and the Longyearbyen GNSS receiver at the Kjell–Henrikson Observatory (KHO) with latitude and longitude values equal to 78.147°, 16.038° respectively. Using data from the ESR 32-m dish operated in a fast scanning mode the dayside auroral/cusp region was monitored during morning hours, which provided *fan plots* of the ionospheric conditions (Carlson et al., 2002). This, together with the GNSS measurements, allowed us to investigate the dominant source region for scintillation causing irregularities. Furthermore, we examined the relation between scintillation and different parameters such as ion and electron temperatures in order to investigate the associated ionospheric conditions during scintillation events. This is useful to reveal the underlying instability mechanisms at different regions which structures the plasma to create the irregularities (Makarevich et al., 2021; Spicher et al., 2020, 2016). A primary understanding of the source region of the density structures is therefore necessary to facilitate further investigation on the type of instability mechanism involved at different altitudes.

The outline of the paper is as follows: Section 2 provides an overview of the data used in the study, Section 3 discusses the methodology employed to identify precise conjunctions between radar beams and GNSS signals, Section 4 presents the results followed by discussions and conclusions in sections 5 and 6, respectively.

2. Data

This study utilizes data collected by the ESR steerable 32-m dish operated in a fast meridional scan with a minimum elevation of 30° above the horizon (Wannberg et al., 1997). One full scan takes about three minutes to complete and yields *fan plots* of electron density (N_e), electron temperature (T_e), ion temperature (T_i) and line-of-sight plasma velocity (V_i) as a function of altitude and latitude, produced with an integration time of 6.4 s (Carlson et al., 2002). The measurements are analysed using the GUISDAP toolbox (Lehtinen and Huuskonen, 1996). In this study, we used data from meridional scans while Svalbard was roughly in the dayside auroral/cusp region during November–December months of 2014 and 2015, and when GNSS satellites from multiple constellations were visible in conjunction with the scans. Information on the dates as well as the start and end times of the radar experiments used in this study can be found in Table 2 of the appendix.

The GNSS data used in this paper correspond to 60-second amplitude and phase scintillation data which were collected by the NovAtel GPStation-6 GNSS Ionospheric Scintillation and TEC Monitors installed at KHO (Oksavik, 2020a). The receiver is capable of simultaneously tracking signals at several different frequencies from different constellations such as GPS, GALILEO and GLONASS (Oksavik, 2020b). More information about data processing can be found in Oksavik et al. (2015) and van der Meeren et al. (2015). This data set is part of The University of Bergen Global Navigation Satellite System Data Collection (Oksavik, 2020c). Scintillation indices, S_4 and σ_ϕ, are used to quantify scintillation where the former quantifies the scintillation in amplitude and the latter in the phase of the radio wave (Yeh and Liu, 1982). These indices are calculated by detrending the raw amplitude and carrier phase with a sixth-order Butterworth low-pass and high-pass filters respectively, in order to remove the low frequency trends in the data which are the result of the satellite motion and long term variations in the ionosphere (Fremouw et al., 1978; Van Dierendonck et al., 1993). By choosing a cut-off of 0.1 Hz, we are effectively removing the contamination of ionospheric information by low frequency trends as much as possible but also making sure that information about larger scale structures, that can also affect GNSS signals, are preserved in the process. It is worth noting that S_4 values are affected by ambient noise and hence should be taken into account during their calculation (Van Dierendonck et al., 1993). S_4 index contains information on Fresnel-sized irregularities and is not sensitive to large-scaled irregularities whereas the phase scintillation index, σ_ϕ, encompasses effects due to both large and Fresnel-scaled irregularities which cause refractive fluctuations and diffractive variations in the signal (McCaffrey and Jayachandran, 2019). This is often manifested as the dominance of σ_ϕ index when compared to the S_4 index especially at high latitudes where the occurrence rate of amplitude scintillation is lower than that of phase scintillation (Meziane et al., 2020). Numerous studies have shown this to be an artifact induced as a result of improper detrending of the signal carrier phase using the conventional cut-off frequency of 0.1 Hz that was found to be more appropriate at low-latitudes (Spogli et al., 2009; Forte and Radicella, 2002; Mushini et al., 2012; McCaffrey and Jayachandran, 2019; Madhanakumar et al., 2022; Wang et al., 2018; Song et al., 2022). Since we want to capture the effects of both large and small-scale irregularities, and hence from both refraction and diffraction, we use the 0.1 Hz detrended phase scintillation index in our study. From here on, scintillation refers to both refractive and diffractive variations as captured by the σ_ϕ index. Data corresponding to L1 frequency of GPS, GALILEO and GLONASS are used for the analysis. Worth pointing out the removal of data from GLONASS 21 as the satellite was providing data of poor quality which was found by comparing the GLONASS 21 data recorded simultaneously at different stations (Ny-Ålesund and Bjørnøya).

3. Methodology

In order to investigate the altitude of scintillation causing irregularities, coinciding GNSS and radar observations are necessary. In this section, we describe the procedure employed to identify conjunctions between the radar and GNSS radio signals at all altitudes. As the first step, radar data which had 30% or more errors were removed from each beam. We then define conjunction between a radar beam and a satellite line-of-sight vector (LOS) as an *event* when their latitudinal and longitudinal separation do not exceed 0.2° and 0.4° respectively, which correspond to about 22 km in extent. These thresholds were chosen to make sure that the radar and the satellite links were looking almost at the same ionospheric region while still providing significant amount of

conjunctions for statistical analysis. Moreover, with an opening angle of ∼ 1°, the spatial resolution obtained at F region altitudes is ∼ 5 km. In this study, the radar antenna was sweeping through ∼ 120° in about three minutes with the data at different altitudes obtained using an integration period of 6.4s. This would therefore give a horizontal spatial resolution of ∼ 35 km at the F region altitudes. The choice of 22 km therefore makes sure that a GNSS conjunction is obtained within the radar viewing region of the ionosphere enabling proper comparison of the two datasets. This criterion is applied to all altitudes and for each beam, starting from 90 km up to the maximum altitude measured in that beam with a step size of 5 km. By doing so we are not making any assumption about the altitude of the ionospheric pierce point (IPP). Worth pointing out that there could be data missing from the radar beams especially at higher altitudes due to different factors such as insufficient electron density for backscatter, satellite passes and naturally enhanced ion-acoustic lines (NEIALs). Therefore, we considered only beams that contain at-least three data points in each of the E and F regions as well as conjunctions up to at-least 300 km for further analysis so as to make an unbiased comparison of irregularities in the two regions.

The above-mentioned procedure is illustrated in Fig. 1, which shows one full scan made by the 32-m ESR on 30 November 2015 between 10:07:47 and 10:10:52 UTC. One full scan is composed of multiple beams (Beam 1 and Beam 7 for instance) having different look directions. The data gaps above 350 km in beams 4 and 5 result from the removal of data with errors ≥ 30%. The horizontal orange dotted line at 150 km in Fig. 1 demarcates the E region from the F region. The magenta trajectory line indicates the satellite LOS vector which intersects some of the radar beams during this particular scan period. Over-plotted as circles and squares are the σ_ϕ and S_4 indices, with the sizes representing the magnitude of the indices (precise values are indicated in the legend at the bottom of the figure). Scintillation data is shown only at specific altitudes to avoid cluttering of datapoints which would otherwise hinder visual clarity. As seen in Fig. 1, two GNSS satellites are in the field of view of the radar but conjunction as defined above occur only until about 200 km for satellite A (Sat A in the figure) whereas it reaches 400 km for Sat B. This is because Sat B remains in the radar scan plane with its (lat,lon) values falling within the (lat,lon) threshold of (± 0.2°, ± 0.4°) of the radar beam up to an altitude of 400 km. On the other hand, the (lat,lon) values of Sat A fall outside the radar scan plane beyond an altitude of around 200 km and hence the satellite trajectory indicated by the magenta line terminates at 200 km.

Unambiguous identification of density structures that cause scintillation is difficult as long as we do not have the full 3D spatio-temporal information of the plasma. However, different proxies have been used to identify density enhancements such as in-situ studies of Dao et al. (2011), Yizengaw et al. (2013) where $\Delta N_e/N_0$ was used to decouple plasma density irregularities from the ambient density (N_0) and was used as an indicator of the strength of density irregularities. Other in-situ studies such as Coley and Heelis (1995) used ion density observations to detect density enhancements such that plasma structures with peak density at least double the mean density were classified as polar cap patches. Using Swarm data (Spicher et al., 2017) identified density enhancements as patches if they exceeded twice the 35th percentile of the plasma density measurements in a 2000 km window. Noja et al. (2013), using CHAMP data, required the peak total electron content (TEC) to be greater than 4 TECU above the background in order to be classified as a density enhancement/patch (Chartier et al., 2018). As far as scintillation in GNSS signals are concerned it is the fluctuation in electron density from the background that becomes important (Yeh and Liu, 1982; Aarons et al., 1981; Kivanç and Heelis, 1997). In addition, sufficient density gradients have to be present within the enhanced plasma for scintillation to occur (Jenner et al., 2020). We therefore simultaneously used both density enhancement from the background as well the presence of associated gradients as indicators for the presence of irregularities that can cause scintillation in GNSS radio signals. The procedure is described below.

Radar scans were used to identify density structures in the ionosphere and hence the density fluctuation (ΔN) was obtained using the following equation:

$$\Delta N = \mathcal{N}_e^i - N_0 \tag{1}$$

Here, $\mathcal{N}_e^i$ represents the electron density in beam i. Since we are interested to identify the source region of irregularities that cause scintillation, the average $\mathcal{N}_e^i$ and hence ΔN were calculated for both E and F regions separately. N_0 is the background density which, for our purpose, was taken to be the average of the envelope of minimum densities recorded in each beams for the entire duration of the experiment, for each of the regions separately. Aarons et al. (1981), Jenner et al. (2020) and van der Meeren et al. (2016) had shown that significant plasma density above the background level have to be present for scintillation to occur at GNSS frequencies. Since our objective is to relate scintillation in GNSS links to irregularities in different ionospheric layers, we therefore required ΔN in each region to exceed its respective background in order for the density enhancement to affect GNSS signals. For instance, density enhancements above the background are present in the E region if the following condition is satisfied:

$$\Delta N^E > N_0^E \tag{2}$$

Eq. (2) can be re-arranged as:

$$\frac{\Delta N^E}{N_0^E} = \Delta \mathcal{N}^E > 1 \tag{3}$$

Similarly, the presence of density enhancement in the F region is indicated by the following condition:

$$\frac{\Delta N^F}{N_0^F} = \Delta \mathcal{N}^F > 1 \tag{4}$$

In addition to the existence of plasma density enhancements, we also required density variations (or gradients), ∇N, to exist within these plasma structures in order to distinguish smooth and uniform density structures from scintillation causing irregularities. This was calculated from consecutive beams using the following equation:

$$\nabla N = \mathcal{N}_e^{i+1} - \mathcal{N}_e^i \tag{5}$$

Similar to the density enhancements, ∇N was calculated for both E and F regions separately. Jenner et al. (2020) had concluded that significant density gradients are a pre-requisite for scintillation to occur at GNSS frequencies along with sufficient plasma densities. Therefore we required ∇N to exceed the background gradient in order for the density enhancement to contain significant gradients (i.e. irregularities) that can affect GNSS signals. For the E region this is given by the following condition:

$$\nabla N^E > N_{\mathcal{O}}'^E \tag{6}$$

where $N_{\mathcal{O}}'^E$ is the background gradient in the E region. Eq. (6) can be re-arranged as:

$$\frac{\nabla N^E}{N_{\mathcal{O}}'^E} = \nabla \mathcal{N}^E > 1 \tag{7}$$

Similarly, the presence of variations (gradients) within density structures of the F region is indicated by the following condition:

$$\frac{\nabla N^F}{N_{\mathcal{O}}'^F} = \nabla \mathcal{N}^F > 1 \tag{8}$$

In summary, in order for a scintillation (or non-scintillation) event to be associated with a particular ionospheric region (eg., the E region) the following conditions have to be simultaneously satisfied:

1. The E region density enhancement has to exceed the background E region density (i.e. $\Delta \mathcal{N}^E > 1$)

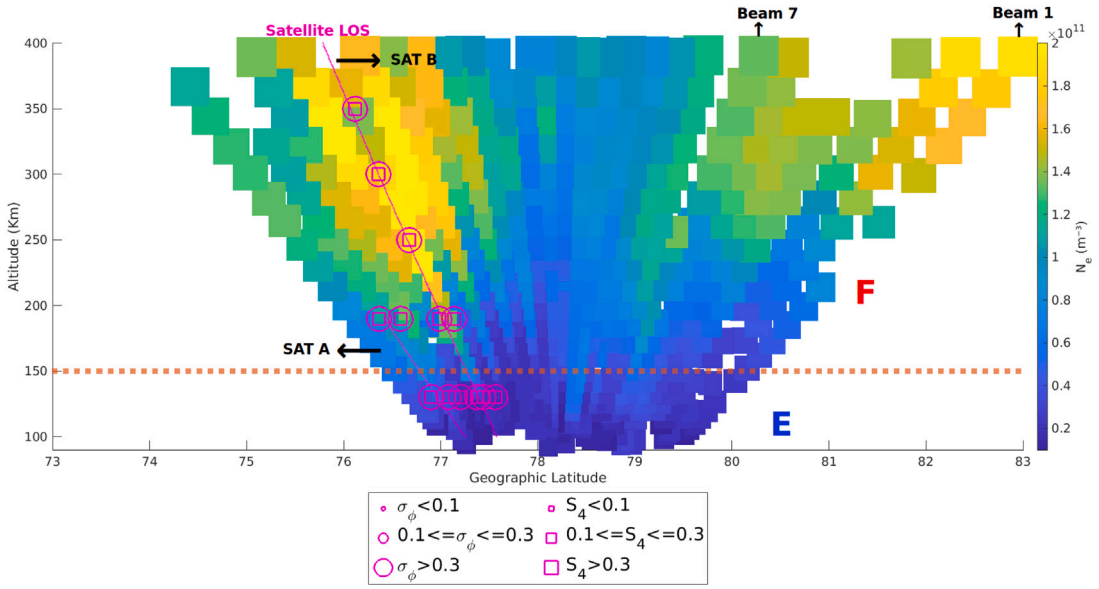

Fig. 1. ESR radar scan from 10:07:47 to 10:10:52 UTC on 30 November 2015 showing the electron density profile as a function of altitude and geographic latitude. Amplitude and phase scintillation indices are overplotted as magenta squares and circles, respectively.

Table 1
Criteria used to classify scintillation events with respect to irregularities in different ionospheric regions.

E	F	E&F	Below background
$\Delta\mathcal{N}^E > 1,\ \nabla\mathcal{N}^E > 1$ & $\Delta\mathcal{N}^E > \Delta\mathcal{N}^F,\ \Delta\mathcal{N}^F < 1$	$\Delta\mathcal{N}^F > 1,\ \nabla\mathcal{N}^F > 1$ & $\Delta\mathcal{N}^F > \Delta\mathcal{N}^E,\ \Delta\mathcal{N}^E < 1$	$\Delta\mathcal{N}^E > 1,\ \nabla\mathcal{N}^E > 1$ & $\Delta\mathcal{N}^F > 1,\ \nabla\mathcal{N}^F > 1$	$\Delta\mathcal{N}^E < 1$ & $\Delta\mathcal{N}^F < 1$

2. The F region density enhancement has to remain below the background (i.e. $\Delta\mathcal{N}^F < 1$)
3. Density enhancement in the E region has to exceed that in the F region (i.e. $\Delta\mathcal{N}^E > \Delta\mathcal{N}^F$)
4. The enhanced density structure should contain significant electron density gradients (i.e. $\nabla\mathcal{N}^E > 1$)

Similar conditions are used to associate the observed scintillation/non-scintillation events with the F region. When a GNSS receiver measures σ_ϕ index exceeding 0.1 rad we classify it as a *scintillation event* whereas events with σ_ϕ below 0.1 rad are classified as *non-scintillation events*. Depending on the region exhibiting irregularities identified using the radar, events are then associated with one of the following four categories during the conjunction period: (1) E region irregularities, (2) F region irregularities, (3) both E and F region irregularities, (4) below the background. Table 1 summarizes the criteria selected behind this classification.

4. Results

The results are divided into two parts: first we study the altitude of the ionospheric source region containing irregularities associated with GNSS scintillation and then we proceed to investigate the ionospheric conditions during such events.

4.1. Ionospheric source regions during GNSS scintillation

The objective here is to present the results of the analysis performed to characterize the relative contributions of irregularities in different ionospheric regions to GNSS scintillation at the dayside auroral/cusp regions. Using the procedure outlined in the methodology section, conjunctions between the ESR and GNSS satellite signals were identified, and the observed scintillation was associated with different regions of the ionosphere. We first present individual case studies when different ionospheric regions exhibited enhanced density enhancements and gradients before presenting the statistical results.

Fig. 2 shows the density enhancement from the background (column I) and the density variations calculated between adjacent beams (column II) with scintillation indices overplotted. These examples illustrate all three categories, i.e. when scintillation was attributed to: "E region" (Fig. 2.a), "F region" (Fig. 2.b), and "E+F region" (Fig. 2c).

On 05 December 2015 (Fig. 2.a), the fan plots (column I) exhibited enhanced densities in the E region equatorward of the radar (radar location at about 78.1°) and enhanced F region densities poleward of the radar. Both the E and F region plasma enhancements contained significant gradients as visible in column II implying the existence of irregularities within the plasma structures. Stronger density enhancements and gradients existed in the E region than the F region when there was conjunction between the radar and satellite signals (region overplotted with magenta circles and squares). The scintillation event observed during this scan is thus classified as an E region event. Fig. 2.b shows enhanced F region structures and density gradients equatorward of the radar on 30 November 2015. During the scan, scintillation coincided with a stronger F region density enhancement. The corresponding plasma density gradients, shown on the right, were strongest in the F region. This event is hence associated with the F region irregularities. On 30 November 2015 (Fig. 2.c), both the E and F regions simultaneously contained strong levels of density enhancements and gradients equatorward of the radar when scintillation was observed. Hence this event is classified as being associated with both E and F region irregularities. Notably, this event was associated with S_4 index exceeding 0.1. Even though the radar could not resolve Fresnel scaled structures, an enhanced S_4 index implies the presence of Fresnel sized irregularities embedded in larger scale-sized density structures.

The procedure of identifying events and associating them to different ionospheric regions were repeated for all the meridional scans listed in Table 2 and with GNSS satellites from all the constellations

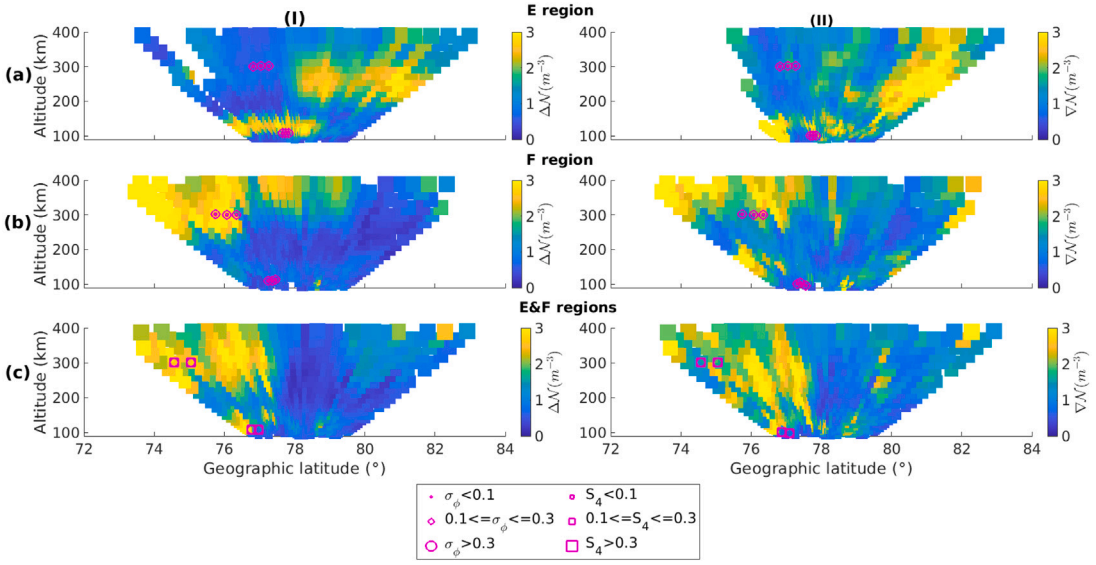

Fig. 2. Density enhancement from the background (column I) and density gradients (column II) from different ionospheric layers with overplotted scintillation levels, as shown in the legend. (a) E region irregularity (scan between 07:28:06–07:31:12 UT), (b) F region irregularity (scan between 10:10:59–10:14:04 UT), (c) E and F irregularities (scan between 08:18:59–08:22:04 UT).

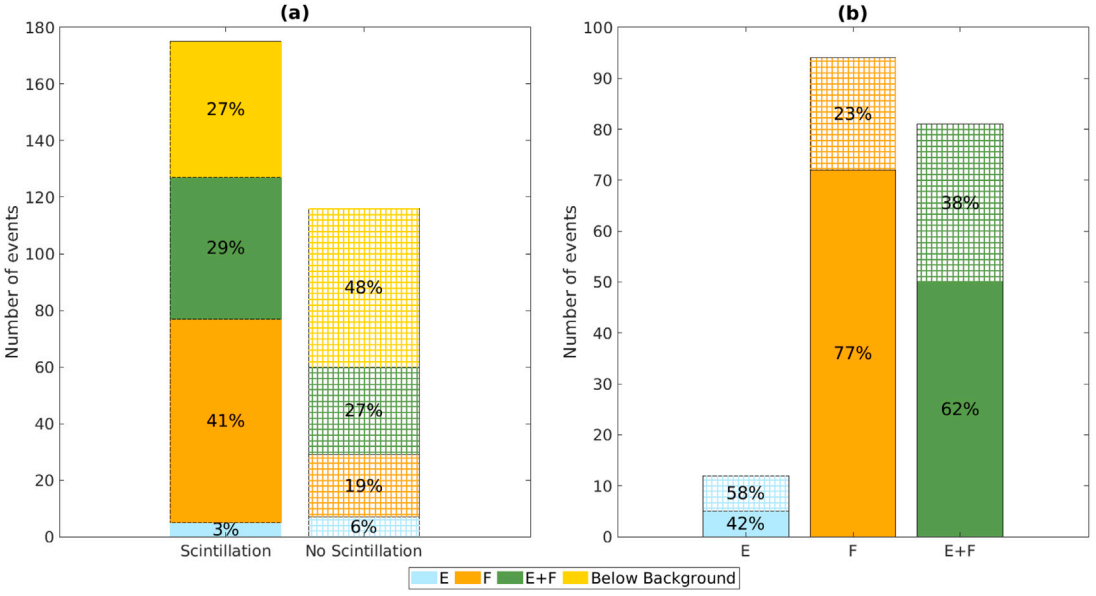

Fig. 3. (a) Contribution of different regions during intervals of scintillation and no scintillation and (b) Occurrence of scintillation and no scintillation, separately for cases when irregularities existed in the E region, F region and both E and F regions simultaneously. The "filled" graphs denote scintillation events whereas the "meshed" graphs denote events when scintillation was absent.

in order to build the statistics. In Fig. 3.a we show the result of the statistical study when scintillation was both present (filled graphs) and absent (meshed graphs) in GNSS signals. A total of 291 conjunction events were identified using the procedure outlined in the methodology section, 175 of which were classified as "scintillation events" and 116 were categorized as "non-scintillation events" (Fig. 3.a). Out of 175 scintillation events, only two exhibited $S_4 > 0.1$ with values of 0.105. The associated noise level recorded by the receiver was 0.031. Consequently, S_4 remained above the threshold of 0.1 even after considering the effect of ambient noise for these two events. Worth pointing out that the number of conjunction events are representative of all the data obtained irrespective of conjunction as shown in Fig. 7 in the appendix.

Fig. 3.a shows that scintillation events were associated with irregularities existing in either one of the regions for about 73% of the time (128 events). Of the 73%, majority of the events were linked with F region irregularities (~ 41%) whereas it was associated with the E region only for about 3% of the cases. During intervals without scintillation, the radar did not detect any irregularities 48% of the times (which increased from 27% during scintillation events). Moreover, the share of the F region decreased from 41% to 19% when there was no scintillation.

Fig. 3.b depicts the occurrence rate of scintillation (filled graphs) and absence of scintillation (meshed graphs) for each ionospheric region separately. From Fig. 3.b it is evident that when the ionosphere predominantly contains F region irregularities, scintillation occurs 77% of the times whereas the likelihood of associating scintillation with E region irregularities are comparatively less. When irregularities were present in both E and F regions simultaneously, the occurrence rate of scintillation is 62%.

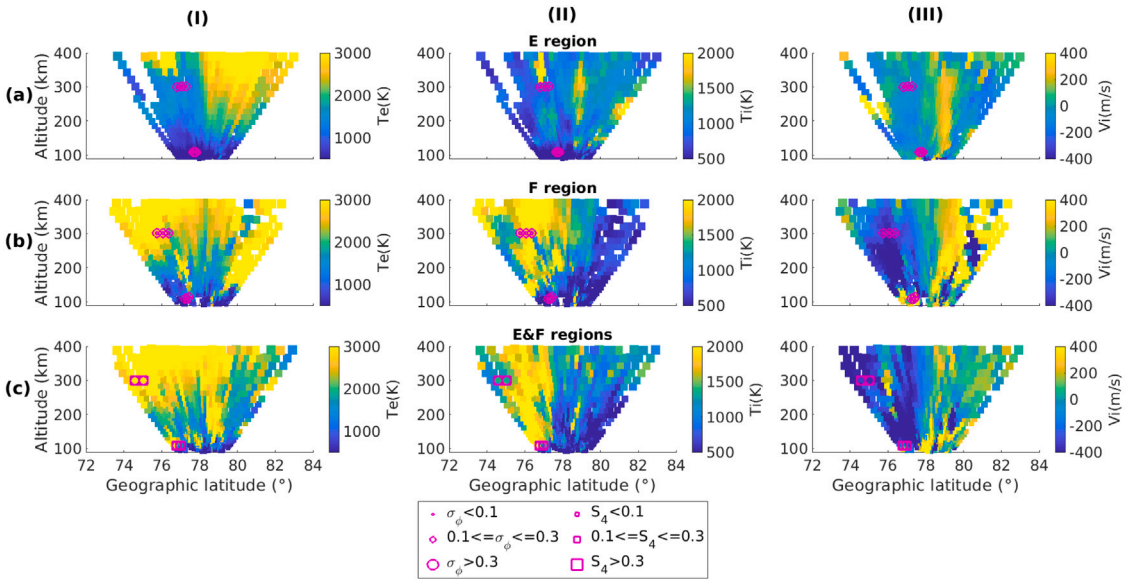

Fig. 4. Scan plots of T_e (left), T_i (middle) and V_i (right) depicting the ionospheric conditions corresponding to Fig. 2, when scintillation was associated with: (a) E region irregularities, (b) F region irregularities, (c) both E and F region irregularities.

4.2. Statistics of the ionospheric conditions during scintillation

In addition to observing ionospheric densities, the radar also gives information about the electron and ion temperatures (T_e and T_i), as well as the line-of-sight plasma velocity (V_i). It is of interest to look at the aforementioned quantities whenever there is scintillation as a relation between enhancement in any of these quantities and the presence of scintillation could be used to identify the underlying instability mechanisms at play. Fig. 4 shows the ionospheric conditions observed by the ESR for the three case studies shown in Fig. 2 with columns (I), (II) and (III) representing T_e, T_i and V_i respectively. Fig. 4.a shows T_e (left), T_i (middle) and V_i (right) when scintillation was associated with E region irregularities (corresponding to Fig. 2.a). During the conjunction interval, the average E region T_i was higher than the average T_e with the former approximately equal to 600 K and the latter equal to 300 K. There was not much flow associated with the E region when scintillation was observed. However, enhanced regions of T_e, T_i and V_i were present poleward of the radar in the F region associated with the enhanced F region density (see Fig. 2.a). The distribution of T_e, T_i and V_i corresponding to Fig. 2.b, i.e. when scintillation was associated with F region irregularities, is shown in Fig. 4.b. Average F region T_e during conjunction was about 4000 K whereas T_i had values around 1700 K. A region of strong flow shear collocated with enhanced T_i was present during scintillation. The presence of enhanced T_i in regions of fast flows can be attributed to Joule heating of the ions (eg.,Skjæveland et al., 2017). Fig. 4.c shows T_e, T_i and V_i corresponding to Fig. 2.c when scintillation was associated with both E and F region irregularities. The average T_e values were about 2000 K and 2500 K for the E and F regions whereas the corresponding T_i values remained around 1600 K for both the regions. Coincident fast flow towards the radar was also present when scintillation was observed. Furthermore, enhanced T_e in both E and F regions were observed poleward of the radar but without much T_i or flows. Worth pointing out that in all three cases, a region of enhanced T_i was present close to where scintillation was observed.

The radar velocity profile only gives information about the line-of-sight velocity whereas T_i may capture effects due to both line-of-sight and transverse flows (see Fig. 4, columns (II) and (III)). We therefore use T_i instead of V_i alongside T_e as indicators to reveal the associated ionospheric conditions during GNSS scintillation. In order to statistically investigate the ionospheric conditions during conjunctions, we analysed the electron and ion temperatures when different regions dominated (i.e. corresponding to the events shown in Fig. 3.b.) The average of T_e and T_i separately for each region represented the electron and ion temperatures in the E and F regions respectively for a given beam. From here on, T_e, T_i represents the average values for the respective regions.

Fig. 5 shows the distribution of σ_ϕ as a function of T_e and T_i when events (scintillation or no scintillation) were associated with (a): E region irregularities, (b): F region irregularities, (c): both E and F region irregularities. When irregularities are present in both the E and F regions simultaneously we take the average of T_i and T_e from both the regions as a representative value. The dotted blue line indicates the $T_i = T_e$ line.

From panels (a,b,c) of Fig. 5 it is seen that events with $\sigma_\phi \geq 0.1$ rad are spread about a wide range of temperature values and are not just concentrated around enhanced T_i or T_e values. In general no statistically significant linear correlation is observed between the level of scintillation indices and any of the ionospheric parameters shown. When the ionosphere contained only E region irregularities (Fig. 5.a), scintillation remained in the weak regime. When scintillation was associated with F region irregularities (Fig. 5.b), over 99% of the events occurred above the $T_i = T_e$ line (blue dotted line). Moreover, enhanced scintillation events with σ_ϕ exceeding 0.3 rad were found to cluster above this line with T_e varying between 2500–4000 K and T_i between 1000–1500 K. Furthermore, when T_e exceeded 2000 K and T_i exceeded 1000 K, about 93% of the events were scintillation with the majority of the non-scintillation events grouped below this value. When irregularities from both the E and F regions were simultaneously present (Fig. 5.c), we again observed enhanced scintillation events with T_e varying between 2500–3000 K and T_i between 1000–1500 K. As with the F region scenario, most of the events occurred above the $T_i = T_e$ line with a majority of the non- scintillation events grouped together below a T_e threshold of 1500 K.

5. Discussion

By taking advantage of the scanning capability of the EISCAT 32-m radar and its co-location with a GNSS receiver in Longyearbyen, we assessed the source region and ionospheric conditions for ionospheric scintillation at the dayside auroral/cusp region. The statistics presented in this study was built by identifying conjunctions between the radar

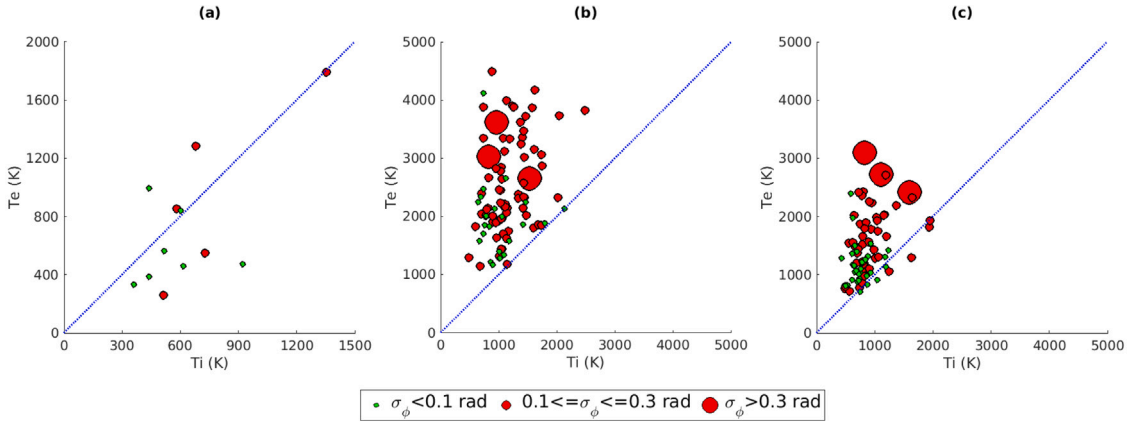

Fig. 5. Distribution of σ_ϕ as a function of electron, ion temperatures when the observed scintillation was associated with irregularities in the: E region (Fig. 5.a), F region (Fig. 5.b) and both E and F regions (Fig. 5.c). The dotted blue line indicates the $T_i = T_e$ line.

and GNSS satellite line-of-sight vectors with a threshold of 0.2° in latitude and 0.4° in longitude at each altitude, without assuming a prior IPP. The chosen thresholds imply that the radar and GNSS signals were observing a common ionospheric region within ∼ 22 km in both latitude and longitude. Different thresholds were tested but the conclusions of the study remained unchanged. Increasing the thresholds would increase the size of the observing region making it more difficult/uncertain to associate the structures visible in the radar to scintillation observed in GNSS links. Moreover, it was also found that increasing the background thresholds in order to identify irregularities based on density enhancements and gradients did not affect the conclusions of this study. Increasing the background threshold to higher values would capture only the effects of stronger irregularities which is useful to identify the relation between GNSS scintillation levels and the strength of irregularities.

Using the conjunction analysis described in the methodology section, scintillation in GNSS signals were associated with different ionospheric regions as observed by the ESR. A total of 175 events were identified as scintillation when σ_ϕ exceeded 0.1 rad. The σ_ϕ index contains information on both small and large scale irregularities, with the major contribution from larger scales due to larger phase fluctuation power (Yeh and Liu, 1982; Kintner et al., 2007). On the other hand, S_4 captures the fluctuations in amplitude of the signal that result from the focusing/defocussing and diffraction effects caused by irregularities with sizes near the first Fresnel zone (Yeh and Liu, 1982; Fremouw et al., 1978). The fact that majority of our events had $S_4 < 0.1$ therefore suggests that σ_ϕ was dominated with high frequency refractive variations. Panel (a) of Fig. 2 features morning side auroral structures when scintillation was associated with E region irregularities. Multiple density enhancements likely associated with discrete auroral arcs separated in latitude are seen during the scan which is typical in the morning magnetic local time (Sandholt et al., 1998). Panel (b) shows the EISCAT data when strong density enhancements and gradients were observed in the F region. Scintillation was hence attributed to F region structures and is a typical example of the cusp footprint. Enhancements in density along with strong gradients were observed in both E and F regions by the radar, as shown in panel (c), when simultaneous scintillation was observed in GNSS links. The universal time range corresponds to that near the transition region between the morning side aurora and the cusp, hence containing irregularities from both the E and F regions as the source of scintillation.

The statistics revealed that when the ionosphere contains F region structures scintillation occurs 77% of the times whereas the likelihood of occurrence of E region irregularities in the dayside polar ionosphere is comparatively very less with the associated scintillation occurring for 42% of the cases. Fig. 6 below shows the average electron density ($\mathcal{N}_e$), density fluctuations/enhancements ($\Delta\mathcal{N}$) as well as density gradient ($\nabla\mathcal{N}$) values, expressed in their absolute magnitudes, when different ionospheric regions were dominated with irregularities. Panels (a), (c) show the distribution of $\mathcal{N}_e$, $\Delta\mathcal{N}$, $\nabla\mathcal{N}$ when the ionosphere was dominated primarily with E region irregularities (blue) and F region irregularities (orange) separately whereas panels (b), (d) depict the distribution of $\mathcal{N}_e$, $\Delta\mathcal{N}$, $\nabla\mathcal{N}$ when the ionosphere simultaneously contained E and F region irregularities.

From panels (a), (c) it is clear that even though irregularities were found to exist in the E region, the average densities, density fluctuations as well as density gradients were still smaller when compared to F region values. This could be the reason why the likelihood of occurrence of E region irregularities and the associated scintillation were very less at the dayside auroral/cusp regions. On the other hand, F region density enhancements and gradients were much higher with the electron densities in the F region differing from the E region by at least a factor of three most of the times. This explains why we observed scintillation majority of the times when the ionosphere was dominated primarily with F region irregularities. Worth pointing out that the electron density values when E region dominated is comparable to the average hole densities reported in Jenner et al. (2020) when phase scintillation was absent and hence is consistent with the findings that significant plasma density levels are required for irregularities to cause scintillation.

Furthermore, the occurrence rate of scintillation was 62% even though the ionosphere contained irregularities in both E and F regions (see Fig. 3.b). Worth noting from panel (b) of Fig. 6 that average densities and density fluctuations in the F region were stronger than the E region when irregularities simultaneously existed in both layers implying that the major contribution came from F region irregularities. However the associated F density gradients (in panel (d)) were smaller when compared to the cases when the ionosphere primarily contained F region irregularities (see panel (c)). On comparing the statistics of 62% with the 77% occurrence rate (i.e. when the ionosphere was active primarily with F region irregularities), the decrease in the scintillation occurrence could then be attributed to the simultaneous presence of E region irregularities. This is in accordance with Heppner (1972), Aarons et al. (1981) where the authors had noted short-circuiting of irregularities in the F region due to the conductance of the E layer. More recently, Takahashi et al. (2022) reported evidences of suppression of irregularities as a result of auroral particle impact in the cusp ionosphere. A sufficient Pedersen conductance in the E region as a result of ionization was suggested to short the F region current thereby suppressing the irregularities (Takahashi et al., 2022). Our study, based on the statistical results, also suggest that the presence of E region irregularities decreases the chances of observing scintillation in the dayside polar ionosphere. As to whether the suppression of irregularities are always the cause for the absence of GNSS scintillation

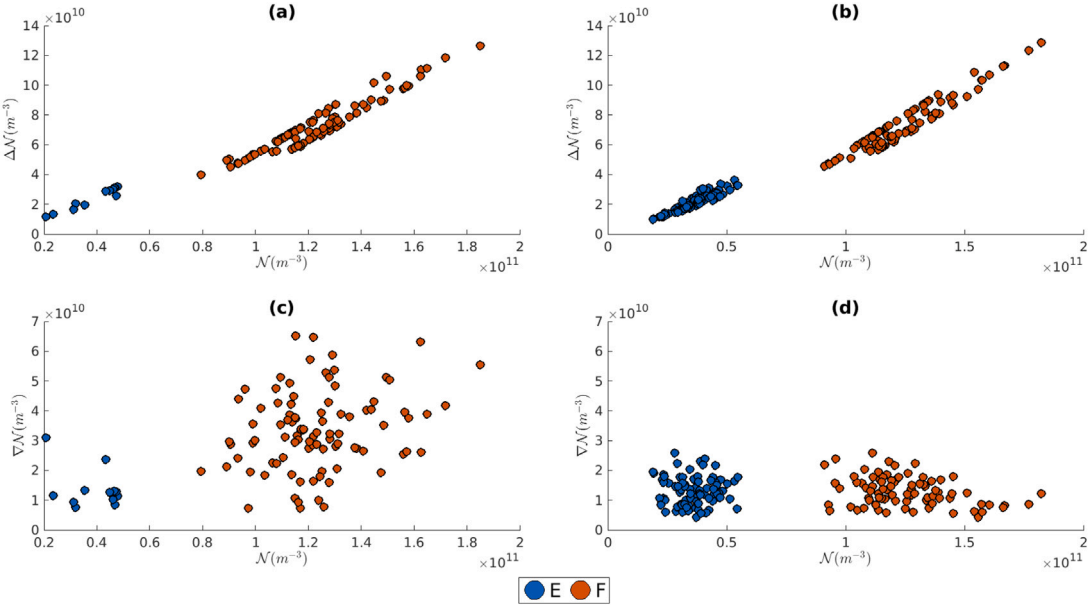

Fig. 6. Panels (a), (c): Distribution of $\mathcal{N}_e$, $\Delta\mathcal{N}$ and $\nabla\mathcal{N}$ when the ionosphere was primarily active with: (i) E region irregularities (blue) and (ii) F region irregularities (orange) respectively. Panels (b), (d): Distribution of $\mathcal{N}_e$, $\Delta\mathcal{N}$ and $\nabla\mathcal{N}$ in the E (blue) and F (orange) regions when irregularities simultaneously existed in both regions. (For interpretation of the references to colour in this figure legend, the reader is referred to the web version of this article.)

would however require more studies before arriving at a definite conclusion. A chi-square test of independence was performed to examine whether the percentages in Fig. 3.b imply a significant difference in the contributions from different regions when scintillation was observed in GNSS signals. The analysis revealed a $\chi^2(3, 291) = 21.5$, $p < .01$ implying that there is a significant difference in the way E and F regions irregularities contribute to scintillation. Evidently the results therefore strongly suggests that F region irregularities are more effective and is the major contributor towards the observed scintillation in GNSS radio waves at the dayside high latitude region.

The statistical results reported here differ from that reported from the night-side sector. Literature found in Semeter et al. (2017), Loucks et al. (2017), Makarevich et al. (2021), Enengl et al. (2023) indicated E region auroral structures to be the main contributor to phase scintillation in GNSS signals at the night-side auroral region. The statistical study in Sreenivash et al. (2020), which used maximum density as an indicator of scintillation causing irregularities, revealed majority of the scintillation events to be due to E region structures. Our methodology, in addition, allows identifying events when both E and F regions can simultaneously contain scintillation causing irregularities. Identifying the source region becomes particularly important for modelling studies where the altitude of the irregularities is an important initial input parameter (Deshpande et al., 2014; Strangeways et al., 2014; Spicher et al., 2020). Instead of assuming a single IPP, modelling studies would then have to take into consideration multiple IPPs during such scintillation events. Worth pointing out that a similar study at the nightside using our methodology would be interesting in order to investigate similarities and differences with the dayside. For the events analysed in this study, σ_ϕ remained in the weak scintillation regime majority of the times irrespective of where the irregularities were present. This could be due to the fact that density enhancements as well as gradients were only moderately high when different regions dominated, as shown in Fig. 6. This is in line with Aarons et al. (1981), Kivanç and Heelis (1997) where the authors had suggested that scintillation intensity depends directly on the density fluctuations/enhancements from the background. Furthermore, our results are also consistent with Jin et al. (2015) where the magnitude of σ_ϕ index was observed to be low during daytime whereas enhanced σ_ϕ was predominant at night-time. Jin et al. (2014, 2016), van der Meeren et al. (2015) had observed the combination of polar cap patches and night-side auroral dynamics (i.e., the combination of E and F structures) to be associated with highest σ_ϕ levels whereas we observed only weak phase scintillation majority of the times when both E and F regions contained irregularities simultaneously. This suggests that the night-side dynamics are more effective than the dayside dynamics in creating enhanced scintillation events.

The associated ionospheric conditions during scintillation as captured by the ion and electron temperatures in Fig. 5 revealed that scintillation occurs about a wide range of temperature values. Identifying the ionospheric conditions during scintillation events would prove helpful to assess different instability mechanisms that might have led to the creation of scintillation causing irregularities. Dominant instability mechanisms at high latitude ionosphere include Kelvin–Helmholtz instability (KHI) (Keskinen et al., 1988; Basu et al., 1988, 1994; Oksavik et al., 2011), Gradient-Drift instability (GDI) (Burston et al., 2009; Weber et al., 1984) and Farley–Buneman instability (FBI) (Farley, 1963; Buneman, 1963). KHI operates when there is a shear in the plasma drift velocity whereas GDI requires a density gradient. FBI is more dominant in the E region and its presence could be inferred from elevated electron temperature values (Bahcivan, 2007; Makarevich et al., 2013; Schlegel and St.-Maurice, 1981). In addition, multiple instability mechanisms can operate together to create density irregularities. Carlson et al. (2007, 2008) had proposed a two-step process wherein KHI acts initially to structure the plasma followed by further structuring to smaller scales by GDI. An alternative two-step process was proposed by Oksavik et al. (2012) wherein an initial particle precipitation created irregularities would be structured further to smaller scales by GDI.

From Fig. 5, it had to be concluded that a statistically significant linear correlation does not exist between any of the ionospheric parameters and σ_ϕ index. Fig. 5.a shows that scintillation always remained in the weak regime when there were primarily E region irregularities. Due to the limited number of E region events we are unable to provide conclusions about the driving mechanism for E region irregularities. More studies are therefore required to discern the relative importance of the different processes in the E region. On the other hand, when the ionosphere predominantly contained F region irregularities (Fig. 5.b), over 99% of the events were observed to lie above the $T_i = T_e$ line. The results suggesting that the ionospheric conditions corresponding

to enhanced T_e and T_i are associated with scintillation majority of the times is in line with the fact that cusp auroral dynamics are an important factor for GNSS scintillation at the dayside auroral region (Jin et al., 2017; Moen et al., 2013). Amongst the possible mechanisms, the dynamics could be associated either with precipitation as discussed in Kelley et al. (1982) where structured soft-electron precipitation was found to be an important source of irregularities in the F region or with fast flows channels (eg., Spicher et al., 2020; Carlson et al., 2002).

Absence of a clear statistical trend between σ_ϕ index and the ionospheric parameters as measured by the radar could be attributed to the fact that the radar is sensitive to only large scale structures, of the order of tens of km and hence is unable to capture the effects due to small scaled irregularities that can cause intense scintillation. In our study, most of the scintillation events were observed to be in the weak regime. Future studies using scintillation data from the moderate and strong regimes would be able to clarify in much more detail as to whether there exists any trend or correlation between scintillation levels as measured by σ_ϕ index and different ionospheric parameters. It could also be due to the fact that the radar observes only 1-D cuts through the ionosphere and hence is not capturing the entire physical picture. EISCAT-3D would prove useful here as it can have multiple look directions simultaneously and is also capable of scanning a single beam through a range of directions repeatedly to build 3-D images of the ionosphere (McCrea et al., 2015). By combining the volumetric imaging capability of EISCAT-3D with GNSS conjunction observations, the full spatio-temporal evolution of irregularities and their associated physical processes that cause scintillation in GNSS radio frequencies can be revealed. The relative effectiveness and contribution of individual instability mechanisms and two-step processes in creating irregularities at different altitudes that can cause scintillation would therefore require more detailed multi-instrument studies.

6. Conclusions and future works

The objective of the study presented here was placed in the context of identifying the ionospheric source region and the associated conditions that produce scintillation in GNSS radio signals in the dayside auroral/cusp region. The purpose was achieved by making use of the scanning capability of the radar and its co-location with a GNSS receiver, allowing to obtain conjunction measurements of radar and satellite links. The results from the analysis revealed that the dayside polar ionosphere was active with F region irregularities majority of the times. Scintillation occurred 77% of the times when F region irregularities were present whereas the likelihood of observing irregularities as well as scintillation associated with the E region were comparatively very small. Lack of significant density, density enhancement from the background as well as electron density gradients are suggested as the reasons for the decreased likelihood of observing irregularities and associated scintillation activity in the E region. The chi-square test of independence showed significant difference in the contributions from the two regions during periods of scintillation and no scintillation. The study therefore strongly suggests that F region irregularities are the dominant source and the major contributor towards the observed GNSS phase scintillation in the dayside polar ionosphere. Moreover, it is also shown that scintillation in the dayside ionosphere can be associated with irregularities simultaneously existing in both E and F regions appreciable number of times with the major contribution from the F region. This becomes important for modelling works and for studies that require separating diffractive and refractive variations from σ_ϕ index, which otherwise assumes a single altitude for the irregularities.

The associated electron and ion temperatures revealed that the occurrence of scintillation is spread about a wide range of temperature values. Enhanced T_e and T_i values in the F region are indicative of the ionospheric state which contain irregularities that can cause scintillation in GNSS signals. The result therefore confirms that cusp auroral dynamics play an important role at the dayside ionosphere in the context of scintillation. Identifying the most likely mechanism and their relative importance in creating scintillation causing irregularities would require more observations and analysis using multi-instruments as presented here aided with in-situ measurements in order to pin down the exact structuring mechanism. Conducting a similar statistical study at the night-side auroral region and with EISCAT-3D is of interest for a future work, which would help reveal the full spatio-temporal characteristics of the irregularities in different regions during scintillation.

Table 2
Radar "fast-scan mode" dates and times with the scan start and end times reported separately.

Date	Scan start time (UTC)	Scan end time (UTC)
20-Nov-2014	06:30:00	08:49:37
24-Nov-2014	09:19:01	10:06:04
29-Nov-2014	06:30:19	07:17:47
02-Dec-2014	06:33:32	09:58:39
03-Dec-2014	06:30:23	08:23:14
04-Dec-2014	06:30:38	09:59:36
05-Dec-2014	06:30:04	10:29:00
07-Dec-2014	06:30:04	07:59:52
27-Nov-2015	06:30:44	10:58:48
28-Nov-2015	06:30:25	10:59:45
29-Nov-2015	09:00:32	10:59:47
30-Nov-2015	06:01:16	10:29:39
02-Dec-2015	06:00:32	10:29:26
05-Dec-2015	06:00:32	10:29:32

CRediT authorship contribution statement

Mahith Madhanakumar: Conceptualization, Formal analysis, Investigation, Methodology, Software, Validation, Visualization, Writing – original draft, Writing – review & editing. **Andres Spicher:** Project administration, Supervision, Writing – review & editing. **Juha Vierinen:** Writing – review & editing, Supervision. **Kjellmar Oksavik:** Data curation, Writing – review & editing.

Declaration of competing interest

The authors declare that they have no known competing financial interests or personal relationships that could have appeared to influence the work reported in this paper.

Data availability

The data is freely available to download and the reference to the data has been given in the manuscript.

Acknowledgements

This research is part of the CASCADE project funded by the Research Council of Norway (RCN) grant 326039. KO was supported by the Research Council of Norway under contract 223252. AS acknowledges the contribution of UiT the Arctic University of Norway to the EISCAT_3D project funded by RCN research infrastructure grant 245683. EISCAT is an international association supported by research organisations in China (CRIRP), Finland (SA), Japan (NIPR and ISEE), Norway (NFR), Sweden (VR), and the United Kingdom (UKRI).

Appendix

See Table 2 and Fig. 7.

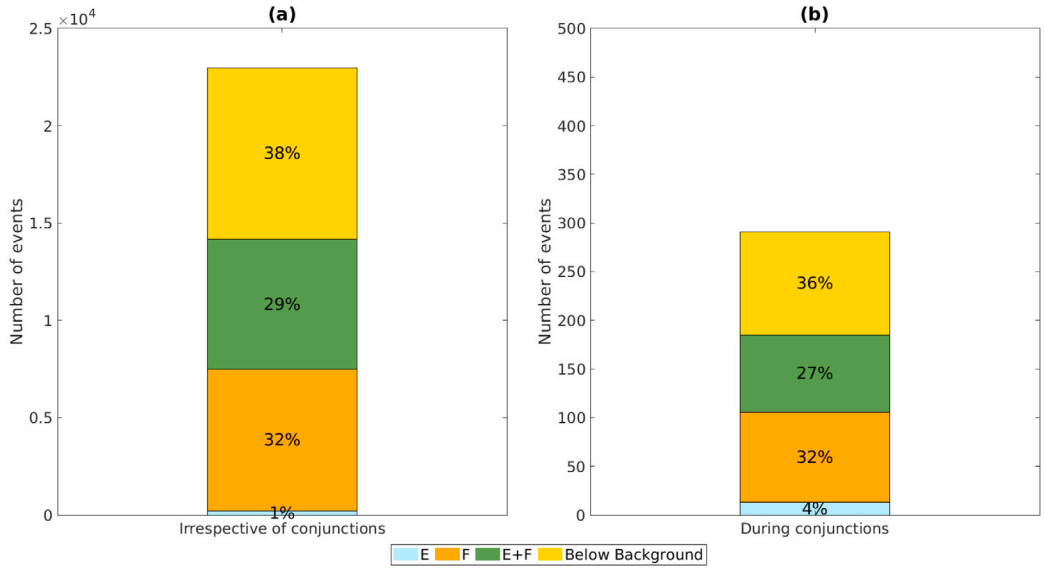

Fig. 7. Relative contributions from different regions using the criteria outlined in Table 1 when: (a) all data irrespective of conjunctions were considered (22977 events) and (b) data during conjunctions between GNSS and radar signals were considered (291 events).

References

Aarons, J., Mullen, J.P., Whitney, H.E., Johnson, A.L., Weber, E.J., 1981. UHF scintillation activity over polar latitudes. Geophys. Res. Lett. 8 (3), 277–280. http://dx.doi.org/10.1029/GL008i003p00277.

Alfonsi, L., Spogli, L., De Franceschi, G., Romano, V., Aquino, M., Dodson, A., Mitchell, C.N., 2011. Bipolar climatology of GPS ionospheric scintillation at solar minimum. Radio Sci. 46 (3), http://dx.doi.org/10.1029/2010RS004571.

Bahcivan, H., 2007. Plasma wave heating during extreme electric fields in the high-latitude E region. Geophys. Res. Lett. 34 (15), http://dx.doi.org/10.1029/2006GL029236.

Basu, S., Basu, S., Chaturvedi, P.K., Bryant, Jr., C.M., 1994. Irregularity structures in the cusp/cleft and polar cap regions. Radio Sci. 29 (1), 195–207. http://dx.doi.org/10.1029/93RS01515.

Basu, S., Basu, S., MacKenzie, E., Fougere, P.F., Coley, W.R., Maynard, N.C., Winningham, J.D., Sugiura, M., Hanson, W.B., Hoegy, W.R., 1988. Simultaneous density and electric field fluctuation spectra associated with velocity shears in the auroral oval. J. Geophys. Res. Space Phys. 93 (A1), 115–136. http://dx.doi.org/10.1029/JA093iA01p00115.

Buneman, O., 1963. Excitation of field aligned sound waves by electron streams. Phys. Rev. Lett. 10, 285–287. http://dx.doi.org/10.1103/PhysRevLett.10.285, URL https://link.aps.org/doi/10.1103/PhysRevLett.10.285.

Burston, R., Astin, I., Mitchell, C., Alfonsi, L., Pedersen, T., Skone, S., 2009. Correlation between scintillation indices and gradient drift wave amplitudes in the northern polar ionosphere. J. Geophys. Res. Space Phys. 114 (A7), http://dx.doi.org/10.1029/2009JA014151.

Carlson, H.C., Oksavik, K., Moen, J., 2008. On a new process for cusp irregularity production. Ann. Geophys. 26 (9), 2871–2885. http://dx.doi.org/10.5194/angeo-26-2871-2008, URL https://angeo.copernicus.org/Articles/26/2871/2008/.

Carlson, H.C., Oksavik, K., Moen, J., van Eyken, A.P., Guio, P., 2002. ESR mapping of polar-cap patches in the dark cusp. Geophys. Res. Lett. 29 (10), 24–1–24–4. http://dx.doi.org/10.1029/2001GL014087.

Carlson, H.C., Pedersen, T., Basu, S., Keskinen, M., Moen, J., 2007. Case for a new process, not mechanism, for cusp irregularity production. J. Geophys. Res. Space Phys. 112 (A11), http://dx.doi.org/10.1029/2007JA012384.

Chartier, A.T., Mitchell, C.N., Miller, E.S., 2018. Annual occurrence rates of ionospheric polar cap patches observed using swarm. J. Geophys. Res. Space Phys. 123 (3), 2327–2335. http://dx.doi.org/10.1002/2017JA024811.

Coley, W.R., Heelis, R.A., 1995. Adaptive identification and characterization of polar ionization patches. J. Geophys. Res. Space Phys. 100 (A12), 23819–23827. http://dx.doi.org/10.1029/95JA02700.

Dao, E., Kelley, M.C., Roddy, P., Retterer, J., Ballenthin, J.O., de La Beaujardiere, O., Su, Y.-J., 2011. Longitudinal and seasonal dependence of nighttime equatorial plasma density irregularities during solar minimum detected on the C/NOFS satellite. Geophys. Res. Lett. 38 (10), http://dx.doi.org/10.1029/2011GL047046.

De Franceschi, G., Alfonsi, L., Romano, V., Aquino, M., Dodson, A., Mitchell, C.N., Spencer, P., Wernik, A.W., 2008. Dynamics of high-latitude patches and associated small-scale irregularities during the October and november 2003 storms. J. Atmos. Sol.-Terr. Phys. 70 (6), 879–888. http://dx.doi.org/10.1016/j.jastp.2007.05.018.

Deshpande, K., Bust, G., Clauer, C., Rino, C., Carrano, C., 2014. Satellite-beacon ionospheric-scintillation global model of the upper atmosphere (SIGMA) I: High-latitude sensitivity study of the model parameters. J. Geophys. Res. Space Phys. 119 (5), 4026–4043. http://dx.doi.org/10.1002/2013JA019699.

Enengl, F., Kotova, D., Jin, Y., Clausen, L.B., Miloch, W.J., 2023. Ionospheric plasma structuring in relation to auroral particle precipitation. J. Space Weather Space Clim. 13, 1. http://dx.doi.org/10.1051/swsc/2022038.

Fæhn Follestad, A., Herlingshaw, K., Ghadjari, H., Knudsen, D.J., McWilliams, K.A., Moen, J.I., Spicher, A., Wu, J., Oksavik, K., 2020. Dayside field-aligned current impacts on ionospheric irregularities. Geophys. Res. Lett. 47 (11), http://dx.doi.org/10.1029/2019GL086722.

Farley, Jr., D.T., 1963. A plasma instability resulting in field-aligned irregularities in the ionosphere. J. Geophys. Res. (1896-1977) 68 (22), 6083–6097. http://dx.doi.org/10.1029/JZ068i022p06083.

Forte, B., Coleman, C., Skone, S., Häggström, I., Mitchell, C., Da Dalt, F., Panicciari, T., Kinrade, J., Bust, G., 2017. Identification of scintillation signatures on GPS signals originating from plasma structures detected with EISCAT incoherent scatter radar along the same line of sight. J. Geophys. Res. Space Phys. 122 (1), 916–931. http://dx.doi.org/10.1002/2016JA023271.

Forte, B., Radicella, S.M., 2002. Problems in data treatment for ionospheric scintillation measurements. Radio Sci. 37 (6), 8–1–8–5, https://agupubs.onlinelibrary.wiley.com/doi/pdf/10.1029/2001RS002508.

Fremouw, E.J., Leadabrand, R.L., Livingston, R.C., Cousins, M.D., Rino, C.L., Fair, B.C., Long, R.A., 1978. Early results from the DNA wideband satellite experiment—Complex-signal scintillation. Radio Sci. 13 (1), 167–187. http://dx.doi.org/10.1029/RS013i001p00167.

Heppner, J., 1972. Electric field variations during substorms: OGO-6 measurements. Planet. Space Sci. 20 (9), 1475–1498. http://dx.doi.org/10.1016/0032-0633(72)90052-9, URL https://www.sciencedirect.com/science/article/pii/0032063372900529.

Hey, J., Parsons, S., Phillips, J., 1946. Fluctuations in cosmic radiation at radio-frequencies. Nature 158, 234. http://dx.doi.org/10.1038/158234a0.

Jenner, L.A., Wood, A.G., Dorrian, G.D., Oksavik, K., Yeoman, T.K., Fogg, A.R., Coster, A.J., 2020. Plasma density gradients at the edge of polar ionospheric holes: The absence of phase scintillation. Ann. Geophys. 38 (2), 575–590. http://dx.doi.org/10.5194/angeo-38-575-2020.

Jin, Y., Miloch, W.J., Moen, J.I., Clausen, L.B., 2018. Solar cycle and seasonal variations of the GPS phase scintillation at high latitudes. J. Space Weather Space Clim. 8, A48. http://dx.doi.org/10.1051/swsc/2018034.

Jin, Y., Moen, J.I., Miloch, W.J., 2014. GPS scintillation effects associated with polar cap patches and substorm auroral activity: Direct comparison. J. Space Weather Space Clim. 4, A23. http://dx.doi.org/10.1051/swsc/2014019.

Jin, Y., Moen, J.I., Miloch, W.J., 2015. On the collocation of the cusp aurora and the GPS phase scintillation: A statistical study. J. Geophys. Res. Space Phys. 120 (10), 9176–9191. http://dx.doi.org/10.1002/2015JA021449.

Jin, Y., Moen, J.I., Miloch, W.J., Clausen, L.B.N., Oksavik, K., 2016. Statistical study of the GNSS phase scintillation associated with two types of auroral blobs. J. Geophys. Res. Space Phys. 121 (5), 4679–4697. http://dx.doi.org/10.1002/2016JA022613, URL https://agupubs.onlinelibrary.wiley.com/doi/abs/10.1002/2016JA022613.

Jin, Y., Moen, J.I., Oksavik, K., Spicher, A., Clausen, L.B., Miloch, W.J., 2017. GPS scintillations associated with cusp dynamics and polar cap patches. J. Space Weather Space Clim. 7, A23. http://dx.doi.org/10.1051/swsc/2017022.

Kelley, M.C., Vickrey, J.F., Carlson, C.W., Torbert, R., 1982. On the origin and spatial extent of high-latitude F region irregularities. J. Geophys. Res. Space Phys. 87 (A6), 4469–4475. http://dx.doi.org/10.1029/JA087iA06p04469.

Keskinen, M.J., Mitchell, H.G., Fedder, J.A., Satyanarayana, P., Zalesak, S.T., Huba, J.D., 1988. Nonlinear evolution of the Kelvin-Helmholtz instability in the high-latitude ionosphere. J. Geophys. Res. Space Phys. 93 (A1), 137–152. http://dx.doi.org/10.1029/JA093iA01p00137.

Kintner, P.M., Ledvina, B.M., de Paula, E.R., 2007. GPS and ionospheric scintillations. Space Weather 5 (9), http://dx.doi.org/10.1029/2006SW000260.

Kivanç, Ö., Heelis, R.A., 1997. Structures in ionospheric number density and velocity associated with polar cap ionization patches. J. Geophys. Res. Space Phys. 102 (A1), 307–318. http://dx.doi.org/10.1029/96JA03141.

Kotova, D., Jin, Y., Spogli, L., Wood, A.G., Urbar, J., Rawlings, J.T., Whittaker, I.C., Alfonsi, L., Clausen, L.B., Høeg, P., Miloch, W.J., 2022. Electron density fluctuations from swarm as a proxy for ground-based scintillation data: A statistical perspective. Adv. Space Res. http://dx.doi.org/10.1016/j.asr.2022.11.042, URL https://www.sciencedirect.com/science/article/pii/S0273117722010742.

Lehtinen, M.S., Huuskonen, A., 1996. General incoherent scatter analysis and GUISDAP. J. Atmos. Terr. Phys. 58 (1), 435–452. http://dx.doi.org/10.1016/0021-9169(95)00047-X, Selected papers from the sixth international Eiscat Workshop..

Loucks, D., Palo, S., Pilinski, M., Crowley, G., Azeem, I., Hampton, D., 2017. High-latitude GPS phase scintillation from E region electron density gradients during the 20–21 december 2015 geomagnetic storm. J. Geophys. Res. Space Phys. 122 (7), 7473–7490. http://dx.doi.org/10.1002/2016JA023839.

Madhanakumar, M., Kashcheyev, A., Jayachandran, P.T., 2022. On the dependence of amplitude and phase scintillation indices on magnetic field aligned angle: A statistical investigation at high latitudes. IEEE Geosci. Remote Sens. Lett. 19, 1–5. http://dx.doi.org/10.1109/LGRS.2021.3115668.

Makarevich, R.A., Crowley, G., Azeem, I., Ngwira, C., Forsythe, V.V., 2021. Auroral E-region as a source region for ionospheric scintillation. J. Geophys. Res. Space Phys. 126 (5), http://dx.doi.org/10.1029/2021JA029212.

Makarevich, R.A., Koustov, A.V., Nicolls, M.J., 2013. Poker flat incoherent scatter radar observations of anomalous electron heating in the E region. Ann. Geophys. 31 (7), 1163–1176. http://dx.doi.org/10.5194/angeo-31-1163-2013.

McCaffrey, A.M., Jayachandran, P., 2019. Determination of the refractive contribution to GPS phase scintillation. J. Geophys. Res. Space Phys. 124, 1454–1469. http://dx.doi.org/10.1029/2018JA025759.

McCrea, I., Aikio, A., Alfonsi, L., et al., 2015. The science case for the EISCAT-3D radar. Progr. Earth Planet. Sci. 2 (21), http://dx.doi.org/10.1186/s40645-015-0051-8.

Meziane, K., Kashcheyev, A., Patra, S., Jayachandran, P.T., Hamza, A.M., 2020. Solar cycle variations of GPS amplitude scintillation for the polar region. Space Weather 18 (8), http://dx.doi.org/10.1029/2019SW002434.

Moen, J.I., Oksavik, K., Alfonsi, L., Daaball, Y., Romano, V., Spogli, L., 2013. Space weather challenges of the polar cap ionosphere. J. Space Weather Space Clim. 3, A02. http://dx.doi.org/10.1051/swsc/2013025.

Mushini, S., Jayachandran, P., Langley, R., MacDougall, J.W., Pokhotelov, D., 2012. Improved amplitude- and phase-scintillation indices derived from wavelet detrended high-latitude GPS data. GPS Solut. 16, 363–373. http://dx.doi.org/10.1007/s10291-011-0238-4.

Noja, M., Stolle, C., Park, J., Lühr, H., 2013. Long-term analysis of ionospheric polar patches based on CHAMP TEC data. Radio Sci. 48 (3), 289–301. http://dx.doi.org/10.1002/rds.20033.

Oksavik, K., 2020a. GNSS Scintillation Data (60 s) at Longyearbyen in 2014. DataverseNO, http://dx.doi.org/10.18710/LZX3MU.

Oksavik, K., 2020b. Documentation of GNSS Total Electron Content and Scintillation Data (60 s) at Svalbard. DataverseNO, http://dx.doi.org/10.18710/EA5BYX.

Oksavik, K., 2020c. The University of Bergen Global Navigation Satellite System Data Collection, DataverseNO. DataverseNO, http://dx.doi.org/10.18710/AJ4S-X394.

Oksavik, K., van der Meeren, C., Lorentzen, D.A., Baddeley, L.J., Moen, J., 2015. Scintillation and loss of signal lock from poleward moving auroral forms in the cusp ionosphere. J. Geophys. Res. Space Phys. 120 (10), 9161–9175. http://dx.doi.org/10.1002/2015JA021528.

Oksavik, K., Moen, J., Lester, M., Bekkeng, T.A., Bekkeng, J.K., 2012. In situ measurements of plasma irregularity growth in the cusp ionosphere. J. Geophys. Res. Space Phys. 117 (A11), http://dx.doi.org/10.1029/2012JA017835.

Oksavik, K., Moen, J.I., Rekaa, E.H., Carlson, H.C., Lester, M., 2011. Reversed flow events in the cusp ionosphere detected by SuperDARN HF radars. J. Geophys. Res. Space Phys. 116 (A12), http://dx.doi.org/10.1029/2011JA016788.

Prikryl, P., Ghoddousi-Fard, R., Kunduri, B.S.R., Thomas, E.G., Coster, A.J., Jayachandran, P.T., Spanswick, E., Danskin, D.W., 2013. GPS phase scintillation and proxy index at high latitudes during a moderate geomagnetic storm. Ann. Geophys. 31 (5), 805–816. http://dx.doi.org/10.5194/angeo-31-805-2013.

Prikryl, P., Jayachandran, P.T., Mushini, S.C., Chadwick, R., 2011. Climatology of GPS phase scintillation and HF radar backscatter for the high-latitude ionosphere under solar minimum conditions. Ann. Geophys. 29 (2), 377–392. http://dx.doi.org/10.5194/angeo-29-377-2011.

Sandholt, P.E., Farrugia, C.J., Moen, J., Noraberg, Ø., Lybekk, B., Sten, T., Hansen, T., 1998. A classification of dayside auroral forms and activities as a function of interplanetary magnetic field orientation. J. Geophys. Res. Space Phys. 103 (A10), 23325–23345. http://dx.doi.org/10.1029/98JA02156.

Schlegel, K., St.-Maurice, J.P., 1981. Anomalous heating of the polar E region by unstable plasma waves 1. observations. J. Geophys. Res. Space Phys. 86 (A3), 1447–1452. http://dx.doi.org/10.1029/JA086iA03p01447.

Semeter, J., Mrak, S., Hirsch, M., Swoboda, J., Akbari, H., Starr, G., Hampton, D., Erickson, P., Lind, F., Coster, A., Pankratius, V., 2017. GPS signal corruption by the discrete aurora: Precise measurements from the mahali experiment. Geophys. Res. Lett. 44 (19), 9539–9546. http://dx.doi.org/10.1002/2017GL073570.

Skjæveland, Å.S., Carlson, H.C., Moen, J.I., 2017. A statistical survey of heat input parameters into the cusp thermosphere. J. Geophys. Res. Space Phys. 122 (9), 9622–9651. http://dx.doi.org/10.1002/2016JA023594.

Smith, A.M., Mitchell, C.N., Watson, R.J., Meggs, R.W., Kintner, P.M., Kauristie, K., Honary, F., 2008. GPS scintillation in the high arctic associated with an auroral arc. Space Weather 6 (3), http://dx.doi.org/10.1029/2007SW000349.

Song, K., Meziane, K., Kashcheyev, A., Jayachandran, P.T., 2022. Multifrequency observation of high latitude scintillation: A comparison with the phase screen model. IEEE Trans. Geosci. Remote Sens. 60, 1–9. http://dx.doi.org/10.1109/TGRS.2021.3113778.

Spicher, A., Clausen, L.B.N., Miloch, W.J., Lofstad, V., Jin, Y., Moen, J.I., 2017. Interhemispheric study of polar cap patch occurrence based on swarm in situ data. J. Geophys. Res. Space Phys. 122 (3), 3837–3851. http://dx.doi.org/10.1002/2016JA023750.

Spicher, A., Deshpande, K., Jin, Y., Oksavik, K., Zettergren, M.D., Clausen, L.B.N., Moen, J.I., Hairston, M.R., Baddeley, L., 2020. On the production of ionospheric irregularities via Kelvin-Helmholtz instability associated with cusp flow channels. J. Geophys. Res. Space Phys. 125 (6), http://dx.doi.org/10.1029/2019JA027734.

Spicher, A., Ilyasov, A.A., Miloch, W.J., Chernyshov, A.A., Clausen, L.B.N., Moen, J.I., Abe, T., Saito, Y., 2016. Reverse flow events and small-scale effects in the cusp ionosphere. J. Geophys. Res. Space Phys. 121 (10), 10,466–10,480. http://dx.doi.org/10.1002/2016JA022999.

Spogli, L., Alfonsi, L., De Franceschi, G., Romano, V., Aquino, M.H.O., Dobson, A., 2009. Climatology of GPS ionospheric scintillations over high latitude and mid-latitude European regions. Ann. Geophys. 27, 3429–3437. http://dx.doi.org/10.5194/angeo-27-3429-2009.

Sreenivash, V., Su, Y., Datta-Barua, S., 2020. Automated ionospheric scattering layer hypothesis generation for detected and classified auroral global positioning system scintillation events. Radio Sci. 55 (1), http://dx.doi.org/10.1029/2018RS006779.

Strangeways, H.J., Zernov, N.N., Gherm, V.E., 2014. Comparison of four methods for transionospheric scintillation evaluation. Radio Sci. 49 (10), 899–909. http://dx.doi.org/10.1002/2014RS005408.

Takahashi, T., Spicher, A., Di Mare, F., Rowland, D.E., Pfaff, R.F., Collier, M.R., Clausen, L.B.N., Moen, J.I., 2022. Suppression of ionospheric irregularity due to auroral particle impact. J. Geophys. Res. Space Phys. 127 (1), http://dx.doi.org/10.1029/2020JA028725.

van der Meeren, C., Oksavik, K., Lorentzen, D.A., Paxton, L.J., Clausen, L.B.N., 2016. Scintillation and irregularities from the nightside part of a sun-aligned polar cap arc. J. Geophys. Res. Space Phys. 121 (6), 5723–5736. http://dx.doi.org/10.1002/2016JA022708.

van der Meeren, C., Oksavik, K., Lorentzen, D.A., Rietveld, M.T., Clausen, L.B.N., 2015. Severe and localized GNSS scintillation at the poleward edge of the nightside auroral oval during intense substorm Aurora. J. Geophys. Res. Space Phys. 120 (12), 10,607–10,621. http://dx.doi.org/10.1002/2015JA021819.

Van Dierendonck, A., Klobuchar, J., Hua, Q., 1993. Ionospheric scintillation monitoring using commercial single frequency C/A code receivers. In: Proceedings of the 6th International Technical Meeting of the Satellite Division of the Institute of Navigation. ION GPS 1993, Salt Lake City, pp. 1333–1342, URL https://api.semanticscholar.org/CorpusID:6671070.

Wang, Y., Zhang, Q.H., Jayachandran, P.T., Moen, J., Xing, Z.-Y., Chadwick, R., et al., 2018. Experimental evidence on the dependence of the standard GPS phase scintillation index on the ionospheric plasma drift around noon sector of the polar ionosphere. J. Geophys. Res. Space Phys. 128, 2370–2378. http://dx.doi.org/10.1002/2017ja024805.

Wannberg, G., Wolf, I., Vanhainen, L.-G., Koskenniemi, K., Röttger, J., Postila, M., Markkanen, J., Jacobsen, R., Stenberg, A., Larsen, R., Eliassen, S., Heck, S., Huuskonen, A., 1997. The EISCAT svalbard radar: A case study in modern incoherent scatter radar system design. Radio Sci. 32 (6), 2283–2307. http://dx.doi.org/10.1029/97RS01803.

Weber, E.J., Buchau, J., Moore, J.G., Sharber, J.R., Livingston, R.C., Winningham, J.D., Reinisch, B.W., 1984. F layer ionization patches in the polar cap. J. Geophys. Res. Space Phys. 89 (A3), 1683–1694. http://dx.doi.org/10.1029/JA089iA03p01683.

Won, J.-H., Lee, J.-S., 2005. A note on the group delay and phase advance phenomenon associated with GPS signal propagation through the ionosphere. Navigation 52 (2), 95–97. http://dx.doi.org/10.1002/j.2161-4296.2005.tb01735.x.

Yeh, K.C., Liu, C.-H., 1982. Radio wave scintillations in the ionosphere. Proc. IEEE 70 (4), 324–360. http://dx.doi.org/10.1109/PROC.1982.12313.

Yizengaw, E., Retterer, J., Pacheco, E.E., Roddy, P., Groves, K., Caton, R., Baki, P., 2013. Postmidnight bubbles and scintillations in the quiet-time june solstice. Geophys. Res. Lett. 40 (21), 5592–5597. http://dx.doi.org/10.1002/2013GL058307.